Monitoring Salt Precipitation in Porous Media Using ^{23}Na MRI: Implications for CO_2 Storage

Naser Ansaribaranghar[1,2], *Mohammad Sadegh* Zamiri[1], *Michael* Dick[3], *Rheya* Rajeev[1,2], *Florea* Marica[1], *Andrés* Ramírez Aguilera[1], *Derrick* Green[3], *Benjamin* Nicot[4], and *Bruce J.* Balcom[1,*]

[1]UNB MRI Research Centre, Physics Department, University of New Brunswick, Fredericton, NB E3B 5A3, Canada
[2]Department of Chemical Engineering, University of New Brunswick, Fredericton, NB E3B 5A3, Canada
[3]Green Imaging, Fredericton, New Brunswick E3A 8V2, Canada
[4]TotalEnergies, Pau, France

Abstract. Salt precipitation, also known as salt-out poses a challenge for CO_2 storage in saline aquifers, due to potential injectivity loss. The primary tool to study this phenomenon in porous media has been X-ray micro-Computed Tomography (X-ray µCT). However, this imaging method uses non-representative fluids and salts to create attenuation contrast. Furthermore, it is limited in field of view and sample size. Magnetic Resonance (MR) offers a non-invasive method for probing salt precipitation using industry-standard core plug samples. ^{23}Na MR/MRI provides quantitative sodium content, which can be combined with ^{1}H MR to give sodium concentration in the brine phase. Experiments were conducted on Bentheimer sandstones saturated with 8 wt% NaCl brine, with dry N_2 as a model gas for CO_2. Salt precipitation was monitored using a variable field magnet allowing to switch between ^{1}H and ^{23}Na MR measurements. The ^{23}Na MR signal was resolved using both T_2* and T_1 relaxation times, enabling quantitative differentiation of sodium content in solution and solid phases. Phase-encode imaging methods were employed to selectively image solution and crystalline sodium. Initially, brine was displaced due to viscous flow of gas. Fluid displacement was well separated from the subsequent evaporation and salt precipitation stages. A complete conversion of the residual solution sodium into crystalline sodium was observed. 1D and 2D images were acquired showing the spatial distribution of sodium during and after drying. Crystallization was localized at the drying front near the sample inlet. This salt accumulation was attributed to capillary backflow to transport sodium to the drying front, as evidenced by the contrasting spatial profiles of ^{23}Na and ^{1}H content in solution. The methods presented using ^{23}Na MRI have a great potential for salt precipitation studies, paving the way for applications in CO_2 storage and other petroleum-related processes.

1 Introduction

Carbon Capture and Storage (CCS) is proposed as a promising strategy for mitigating the impacts of climate change [1] by reducing atmospheric concentrations of carbon dioxide (CO_2). One of the most effective approaches is storage of CO_2 in deep geological formations, such as saline aquifers [2]. These underground reservoirs can offer secure long-term traps for large quantities of CO_2.

To be considered suitable for CO_2 storage, a site must meet several key criteria. (1) A storage site must be in proximity to CO_2 sources, (2) It must provide sufficient storage capacity to accommodate the high volumes of CO_2 required for large-scale operations. (3) Low leakage potential is essential to provide a geological seal that effectively prevents the upward migration of CO_2 plum. (4) High well injectivity is required to allow CO_2 injections at high flow rates [3].

Injectivity plays a crucial role in determining the feasibility and efficiency of a storage operation. Injectivity is primarily influenced by the permeability and porosity of the reservoir rock. However, it is a dynamic property that may decline due to various physical and chemical processes occurring in the reservoir and near the wellbore. One potential challenge to maintaining CO_2 injectivity is the risk of salt precipitation near the wellbore regions [4,5,6]. Salt precipitations have been reported in field operations during gas injection and storage [6,7], resulting in dramatic injectivity reduction.

When dry or under saturated CO_2 is injected into a brine-saturated reservoir, it causes water to evaporate into the CO_2 phase. This evaporation leads to salt concentration buildup. Once the concentration exceeds the salt solubility, precipitates may plug the rock's pore space and reduce permeability. This process may impair the overall injectivity near the wellbore.

However, contradictory results regarding the impact of salt precipitation during CO_2 injection have been reported. Some have reported substantial reductions in the relative permeability to CO_2, while others have observed no significant effect. This apparent contradiction arises

---

[*] Corresponding author: bjb@unb.ca

because, although absolute permeability to all phases may decrease due to pore clogging, the effective permeability to CO_2 can sometimes improve as brine saturation decreases during drying, enhancing CO_2 effective permeability [8]. Ott et al. (2015) attributed these discrepancies to potential dependencies on rock type and specific process conditions [9]. This emphasizes the importance of conducting experiments tailored to the characteristics of the sequestration operation and reservoir fluid properties. Several experimental and numerical studies have confirmed this phenomenon in the context of CO_2 storage [10-14].

During dry or under-saturated CO_2 injection, brine is initially displaced primarily through advective transport. Upon reaching irreducible water saturation, evaporation becomes the dominant mechanism, causing further water removal and salt deposition. Under high-salinity conditions, significant salt deposition can occur. The CO_2 flow rate, drying and salt deposition rates, and spatial distribution of precipitated salts influence the extent and pattern of salt accumulation and therefore well injectivity [8,9]. Understanding the interplay of these parameters under specific reservoir and operational conditions is essential. Consequently, systematic studies of salt precipitation under varying sequestration scenarios are necessary for designing efficient CO_2 injection and salt mitigation strategies.

Flow-through drying of porous media involves four simultaneous mass transfer processes: (1) evaporation of water into the gas phase, (2) solute transport across the medium, (3) conversion of solute to the solid phase, and (4) brine transport across the medium. The latter process is known to be driven by the capillary pressure and is responsible for transporting solutes toward the deposition front [9]. A thorough understanding of these transport mechanisms is essential for predicting the impact of salt deposition on injectivity. If a large quantity of salt is distributed over a substantial length of the porous medium, the effect on injectivity may be minimal. However, if the same quantity of salt accumulates at the deposition front, a significant reduction in injectivity can occur. Thus, the interplay between the mass transfer rates of these processes governs the spatial distribution of salt deposits and ultimately determines the severity of injectivity loss.

Experimental detection of salt formation is challenging. Besides bulk mass measurements and effluent compositional analyses [15], spatially resolved data offer insight into salt-out dynamics. Various experimental tools have been employed to study salt-out, including SEM [16], X-ray µCT, ICP-AES, direct imaging of transparent micro-model [17]. Micro-model imaging [18,19] and X-ray µCT [8,9,20-22] are among the most common techniques used to visualize salt precipitation. Micro-models serve as simplified representations of porous media, allowing controlled studies of flow and precipitation mechanisms. In contrast, X-ray µCT is typically applied to natural rock samples, allowing direct observation of the solid phase. However, X-ray µCT imaging requires sufficient contrast between phases, which is often difficult to achieve with natural fluids and precipitated salts such as halite (NaCl). To achieve sufficient segmentation, salts with higher X-ray attenuation properties and doped fluids are sometimes employed despite halite being the predominant salt observed in field-scale operations. Additionally, the limited field of view (FOV) of X-ray µCT constrains the scale of observations.

Alternatively, Magnetic Resonance (MR) and Magnetic Resonance Imaging (MRI) are non-invasive tools capable of spatial and temporal quantitative measurement. ^{1}H MR has been used to monitor drying in porous media [23]. ^{23}Na MR/MRI, a more recent development [24-26], enables the detection and differentiation of ^{23}Na in the solid and liquid phases, offering a powerful technique for studying salt precipitation dynamics.

MR relaxation times, longitudinal relaxation time (T_1), transverse relaxation time (T_2), and effective transverse relaxation time (T_2*) are sensitive to molecular environment. Sodium in solution and solid are in a significantly different environment yielding different relaxation properties. Solution ^{23}Na shows a short T_1 and a long T_2*, while crystalline ^{23}Na has a long T_1 and short T_2*. This behavior is characteristic of solid MR signals and was exploited for signal separation and selective imaging [27,28]. This allows resolution of the MR signal for sodium in solid and liquid phases.

In this work, salt precipitation in Bentheimer sandstone during N_2 gas injection was monitored using ^{23}Na MR/MRI. N_2 was used as a model gas for CO_2. The ^{23}Na MR signal was resolved through both T_2* and T_1 to give quantitative sodium content in solution and solid phase. Phase encode imaging techniques [29] were used to selectively image either solution or crystalline ^{23}Na. 1D and 2D images were acquired to explore macroscopic effects during the process.

It was found that the initial displacement of brine due to viscous forces is well separated from evaporation and the subsequent salt deposition. The residual NaCl in the core plug, after the initial fluid displacement, remained within the sample, and a complete conversion of dissolved salt into crystalline form was observed. Solution ^{23}Na images showed transport of sodium to the drying front at the sample entrance where salt-out occurred. The mechanism for this transport was found to be capillary backflow. Higher solution ^{23}Na concentration at the entrance was recorded combining ^{1}H and ^{23}Na MRI. The ^{1}H profile showed an opposite trend to that of ^{23}Na.

The methods demonstrated in this work are well suited to probe the flow-through salt-out phenomenon. These methods are non-invasive and give quantitative solution and crystalline ^{23}Na content. The combined use of ^{1}H and ^{23}Na MR/MRI not only quantifies brine and solid salt content but also gives sodium concentration in the solution phase.

Furthermore, there is potential to extend these methods by incorporating ^{13}C MR [30-32] to directly observe CO_2 [33] during the evaporation of water into the injected CO_2 phase, providing complementary information on multiphase distribution and dynamics.

2 Methodology

2.1 Experimental Procedure

Core plugs were cut from a slab provided by Kocurek Industries Inc. (Caldwell, TX). The core plugs were washed with isopropanol alcohol in the Dean-Stark instrument to remove any salt prior to the measurements. Samples were placed in an oven set at 80 °C until the mass remained constant. The samples were then saturated with the brine. Fully brine saturated core plugs were placed in a low-pressure core holder assembled using a Viton sleeve and distributors. Two layers of heat shrink tubing were applied to provide one atmosphere confining pressure and ensuring one-dimensional flow. A steady N_2 flow of 0.25 SCFH was provided using a N_2 cylinder. The laboratory temperature was 20 °C. Capillary number for this experiment was estimated to be $Ca \cong 2.7 \times 10^{-5}$.

2.2 Rocks and Fluids

Dry nitrogen gas was used as a model fluid for CO_2. N_2 was injected at room temperature. 8 wt% NaCl brine was used. A brine density of 1.051 g/ml was measured. Rock samples and their properties are shown in Table I.

Table I. Rock properties

Lithology	Oven-dried mass [g]	Porosity [fraction]	Length [mm]	Diameter [mm]
Bentheimer	116.09	0.24	51	37

2.3 MR/MRI instrument

MR/MRI measurements were conducted using a variable field Cryogen Free Superconducting magnet (MR Solutions, Guildford, Surrey, UK). The magnet was permanently connected to a power supply (Cryomagnetics, Inc., TN, US), allowing change of magnetic field to probe various nuclei at a common frequency. The applied magnetic field was set at 2.99 and 0.79 T for ^{23}Na and ^{1}H, respectively, with a common resonance frequency of 33.7 MHz. A custom-built birdcage RF probe was used for both nuclei. The 90° pulse length was 10 and 40 µs for the ^{1}H and ^{23}Na measurements, respectively. The probe deadtime was 115 µs. The 3D gradient coil was driven by gradient amplifiers (Performance Controls, Inc., PA, US), providing maximum gradient strengths of 66.4, 64.9 and 87.8 G/cm in the three principal directions.

2.4 Theory of MR Signal

Upon insertion of the sample into a magnetic field, ^{1}H and ^{23}Na nuclei are polarized, resulting in a net macroscopic magnetization, M_0 within the sample. This equilibrium magnetization is given by [34]:

$$M_0 = N\frac{\gamma\hbar^2 I(I+1)}{3kT}\gamma B_0 \quad (1)$$

where N is quantity of the nuclei, γ is the gyromagnetic ratio, $\hbar$ is the reduced Plank's constant, I is the spin quantum number, k is the Boltzmann constant, T is the absolute temperature, and B_0 is the static magnetic field. Using the variable field magnet, different nuclei can be studied by changing B_0 to maintain a constant Larmor frequency, $\omega_0 = \gamma B_0$. Therefore,

$$M_0 \propto N\gamma I(I+1) \quad (2)$$

The detected MR signal amplitude, $|s|$, which arises from the electromotive force induced in the receive coil, is described by [34]:

$$|s| = \omega_0 M_0 B_1 V_s \quad (3)$$

where V_s is sample volume and B_1 is the magnitude of the circularly polarized field generated by the RF coil. When measurements are conducted at the same Larmor frequency and using the same RF hardware and probe setup as enabled by the variable field magnet, the MR signal amplitude simplifies to:

$$|s| \propto N\gamma I(I+1) \quad (4)$$

When measuring different nuclei, Eq. 4 can be used to correct the signal for differences in gyromagnetic ratio and spin quantum number. This allows the signal to reflect the actual number of nuclei in the sample. In a brine system, once the number of ^{1}H and ^{23}Na nuclei is known, the sodium concentration can be determined by comparing the two.

2.5 MR Measurements

^{23}Na MR/MRI measurements were performed to track sodium in solid and liquid phase, while ^{1}H MR/MRI was used to track brine. These measurements were repeated over time to monitor the dynamic process. GIT systems software (Green Imaging, Inc., NB, Canada) was employed to execute imaging measurements.

^{23}Na FID measurement provided the total ^{23}Na content. The FID was acquired using a 90° RF pulse. After the deadtime, 4096 data points with a dwell time of 2.5 µs were acquired. Sixteen signal averages were performed with a repetition delay of 100 seconds. Each FID measurement took 27 mins.

^{23}Na T_1 measurement was performed using a saturation recovery method consisted of two parts. In the first part, a comb of 90° pulses were applied to diminish the longitudinal magnetization, followed by a T_1 recovery time, τ_r. In the second part, a 90° pulse was applied, and the signal was acquired with a dwell time of 2.5 µs. τ_r was varied logarithmically 20 times from 1 ms to 100 seconds. Eight signal averages were performed for each τ_r with a repetition delay of 1 second. Each T_1 measurement took 32 minutes.

Details of imaging methods used in this work are provided elsewhere [29]. Hybrid SESPI imaging was used to acquire images of sodium in the liquid phase. This imaging method acquires the reciprocal space data by separate phase encoding of each echo. The echo time was 5 ms, sufficiently long to ensure full decay of the solid signal. Seven time-domain data points acquired at the peak of each echo were averaged to increase the Signal-to-Noise Ratio (SNR). Images had a FOV of 9 cm and 64 number of pixels. A repetition delay of 1 second and 256 signal averages were used. Each measurement took approximately 9 minutes.

The solid phase images were acquired using the 1D DHK SPRITE imaging method [35,36] with an encoding time of 175 µs. 64 signal averages were performed. Images had a FOV of 9 cm and 64 pixels. Each solid phase image was obtained by sequentially acquiring two 1D DHK SPRITE images and subtracting them to isolate the solid phase signal. The first image was acquired with a repetition delay of 1 second and 4 dummy scans prior to the actual acquisition. The short repetition delay and dummy scans suppressed the solid signal. This measurement took 3 minutes. The second image was acquired with a repetition delay of 32 seconds, allowing signal recovery of the solid phase. This measurement took 1 hour and 10 minutes. Subtracting these two images yielded the solid phase image.

Hybrid SESPI imaging was employed for ^{1}H imaging measurements. The echo time was set to 5 ms. To improve SNR, 7 time-domain data points were acquired at each echo and averaged. The imaging FOV was 9 cm, with a spatial resolution of 64 pixels. A repetition delay of 10 seconds and 16 signal averages per measurement resulted in a total acquisition time of approximately 6 minutes.

2.6 Processing

The ^{23}Na FID signal of brine exhibited a slow exponential decay, whereas the signal of NaCl crystals followed a fast-decaying Sinc-Gaussian behaviour. This distinct decay characteristics allowed for differentiation between sodium in the liquid and solid phases. To determine the signal intensity of each signal component, the corresponding decay models were fitted to the acquired FID data. When both dissolved and solid phase sodium coexisted, a simultaneous exponential and Sinc-Gaussian decay function was employed. This fitting procedure follows the methodology described by Guo et al. [37].

For ^{23}Na T_1 saturation recovery, similar to the ^{23}Na FID, the time-domain data points acquired for each T_1 delay was fitted to the appropriate signal model and was back-extrapolated to time zero. This time zero data was then used in a Fast Laplace Inversion algorithm (Laplace Inversion Software, Schlumberger-Doll Research) [38] written in the MATLAB environment (MathWorks, Natick, MA) to produce T_1 relaxation distributions.

An extensive in-house function library in the MATLAB environment, developed using an array-oriented programming language, was employed for data processing. Image reconstruction was performed in MATLAB by applying a Hamming filter to the reciprocal space data, followed by a Fourier transform to generate images.

3 Results and Discussions

The results presented here correspond to one Bentheimer sample. Two additional experiments were conducted on a second Bentheimer and a Berea core plug, which produced similar results. These additional data are not shown to avoid redundancy, but they support the reproducibility of the observations.

3.1 Sodium Content Images

Figure 1 shows 1D images of sodium in the brine. The signal images were calibrated using a reference sample with known sodium content to convert MR signal to mass of NaCl. It is essential to note that these images represent solution sodium rather than brine. As shown in Section 3.5, brine content may be measured using ^{1}H MR measurement. Initially, the sample was fully saturated with brine showing a uniform sodium content across the sample. Upon the introduction of gas flow, brine displacement occurred. The resulting sodium profile immediately after the displacement shows the capillary end effect. The fluid displacement is fast compared to the subsequent stages of evaporation and salt preparation. This observation is consistent with previous studies [9,39,40]. The volume of displaced brine was measured at the effluent to be 4.8 ml. Assuming no change in sodium concentration during this initial displacement step, the difference between the first two ^{23}Na MRI images shown in Figure 1 can be used to also estimate the volume of displaced fluid, yielding a value of 4.7 ml. This is in excellent agreement with the measurement at the effluent. Following the initial displacement phase, the sodium solution content increases near the sample entrance while it simultaneously decreases toward the outlet end. By approximately day 2.5, the sodium content at the sample entrance reaches its peak. Subsequently, ongoing evaporation drives salt precipitation, resulting in a gradual reduction of the solution sodium content until it is entirely depleted throughout the sample.

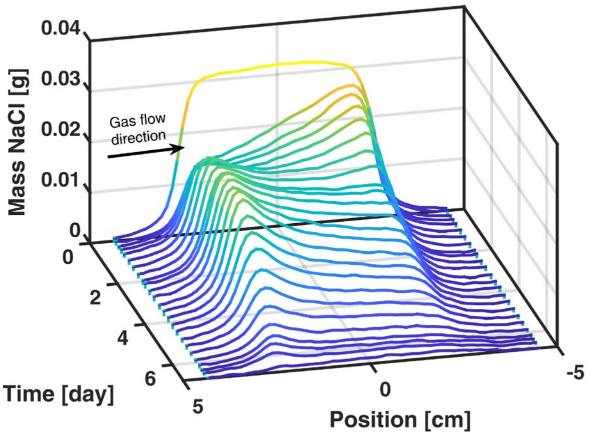

Fig. 1. 1D Hybrid-SESPI images of solution ^{23}Na converted to NaCl mass. The initial profile corresponds to the fully saturated state. Immediately following the displacement, the profile shows the capillary end effect. The subsequent images of the NaCl solution illustrates sodium transport toward the inlet, where deposition occurs.

This peculiar behaviour can be explained by a phenomenon known as capillary backflow [9]. Following the initial displacement phase, evaporation becomes the dominant mechanism. The driving force for evaporation is greatest at the inlet of the sample, leading to localized evaporation at this region. Simultaneously, the capillary pressure is highest at the entrance of the core plug immediately after displacement. The capillary-driven transport dominates over viscous flow in this regime. Therefore, capillary force draws brine toward the inlet, and the sodium solution content at the inlet increases. The peak at the entrance on day 2.5 marks the onset of salt precipitation. The onset of salt precipitation is discussed in Section 3.3. Hereafter, further evaporation causes salt deposition which reduces the solute content in the sample. A systematic investigation of flow rate effects and the associated transition between capillary- and viscosity-dominated regimes is an important direction for future studies.

It is important to note that the Hybrid-SESPI images are influenced by changes in the T_2 relaxation time during the drying process. CPMG measurements (results not shown here) showed that the ^{23}Na T_2 logarithmic mean reduced from 32 ms in the fully saturated state to 10 ms at later stages of drying. This decrease in T_2 affects image intensity and should be considered for quantitative interpretation of the image signal. Furthermore, the evolution of T_2 may contain pore scale information on pore occupancy of sodium while depositing. Therefore, T_2 may provide insights into the mechanisms of salt deposition at the microscopic scale.

3.2 Salt Precipitation Images

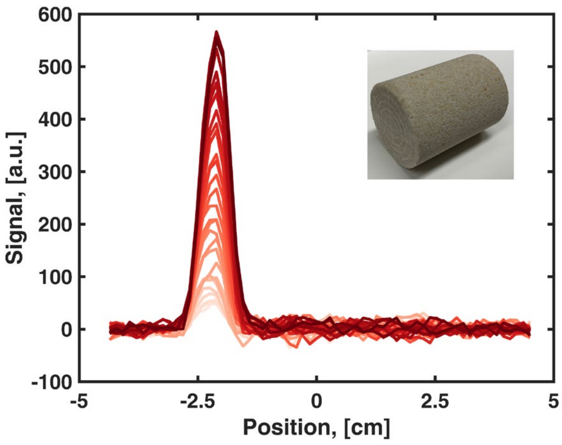

Fig. 2. 1D images of crystalline sodium in the core plug at various times during the process. Each image was generated by subtracting a SPRITE image acquired with a long repetition delay, capturing ^{23}Na in both solid and liquid phases from a SPRITE image acquired with a short repetition delay capturing ^{23}Na in liquid phase. The images show progressive accumulation of salt crystals at the entrance of the core plug. Darker shades correspond to later stages of the process. The inset figure shows the salt deposition at the face of the core plug. Imaging of crystalline sodium began at $t = 2.4$ days and was subsequently performed at 4 hour intervals.

Imaging of the solid phase sodium characterizes the spatial distribution of salt deposition within the sample. Figure 2 illustrates the progressive accumulation of NaCl crystals at the inlet of the core plug. This region of the sample is the primary drying front. This observation aligns with the fact that the entrance experiences the highest evaporation driving force, as the incoming gas is driest at this point. As the gas traverses the porous medium, it becomes increasingly saturated with moisture, thereby reducing the local evaporation potential. A localized or more uniformly distributed pattern of salt crystal accumulation may depend on the gas flow rate [9]. Notably, the buildup of salt at the inlet could lead to injectivity impairment. A systematic variation of the capillary number through controlled changes in flow rate would be valuable for investigating its influence on the location of the drying front and is recommended for future studies. Additionally, further investigation, including simultaneous measurements of effective permeability to CO_2 is necessary to evaluate the impact of salt deposition on CO_2 transport properties.

3.3 Sodium Content Resolved Using T_2* Relaxation Time

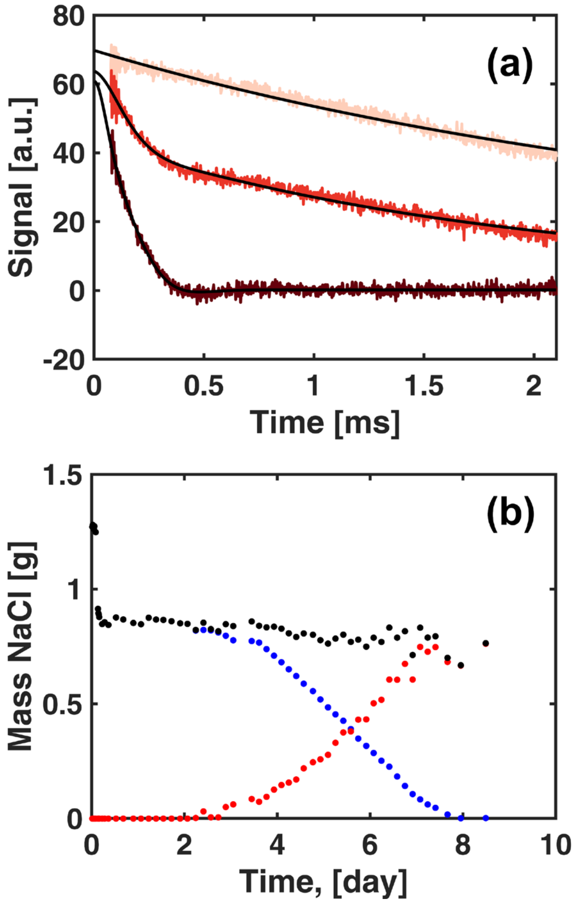

Fig. 3. (a) ^{23}Na FID at three time points. Darker shades correspond to later stages of the process. ^{23}Na FID (▬) initially shows a single exponential decay with a long T_2* time constant. As deposition commences, the FID (▬) shows a short T_2* decay with simultaneous exponential and Sinc-Gaussian behaviours corresponding to ^{23}Na in solution and salt crystals, respectively. After drying is complete, the FID (▬) shows a pure Sinc-Gaussian behaviour. These FIDs were fitted to a mixed simultaneous exponential and Sinc-Gaussian kernel. The

regularization parameter used for the inversion was chosen using the Chi-squared test. The fitted curves were then used to back-extrapolate to time zero. (b) ^{23}Na FID signal intensity resolved using T_2* as a function of time. Data points (●) correspond to solution NaCl, while data points (●) correspond to crystalline NaCl. Data points (●) represent the total NaCl within the sample.

Figure 3(a) shows ^{23}Na FID at three time points of the drying/salt deposition process. Prior to the onset of salt precipitation, solution sodium shows a long T_2* of 4.2 ms. As drying progresses, both solution and crystalline sodium coexist. This causes a distinct signal component corresponding to sodium in salt crystals with a shorter T_2* of 253 µs to emerge. This difference in T_2* is used to resolve and quantify the ^{23}Na MR signal for sodium in crystals and in solution. This quantitative ^{23}Na MR signal was then calibrated using a reference sample with known ^{23}Na content.

Figure 3(b) presents the NaCl content of the entire sample over time, as measured by ^{23}Na FID measurement. The initial decline in NaCl content corresponds to the brine displacement during the early stage of the experiment. Prior to t = 2.5 days, water evaporation occurred without salt precipitation. However, following this time point, salt crystallization began.

Figure 3(b) shows that the total sodium content remains constant throughout the evaporation and deposition. This confirms complete conversion of dissolved salt to salt crystals and validates the quantitative accuracy of the measurements. The observed decrease in dissolved sodium directly corresponds to the increase in solid phase sodium. Furthermore, the sample mass was measured after completion of the process. It exhibited a net mass gain of 0.8 g compared to its post-oven-dried mass. This mass increase corresponds precisely to the amount of salt crystals quantified independently through MR measurements.

Although it might be expected that salt deposition would accelerate as drying progresses, the data in Figure 3(b) indicate that the rate of salt deposition remains approximately constant over much of the experiment. This suggests that the conditions governing evaporation and the subsequent salt precipitation reach a quasi-steady state. As shown in Figure 2, salt deposition is localized to a narrow region at the entrance of the core plug. Sodium is transported toward this region, where precipitation predominantly occurs. The confinement of salt deposition to this localized front likely contributes to the steady deposition rate observed.

3.4 Sodium Content Resolved Using T_1 Relaxation Time

In addition to T_2* contrast, a T_1 relaxation time contrast exists between sodium in solution and solid phase that can be used to distinguish ^{23}Na MR signal components. Figure 4(a) shows the evolution of T_1 recovery curves during the process. As crystallization progresses, signal recovery at shorter recovery delays, τ_r diminishes, while increased recovery is observed at longer τ_r values. This indicates growing solid phase sodium.

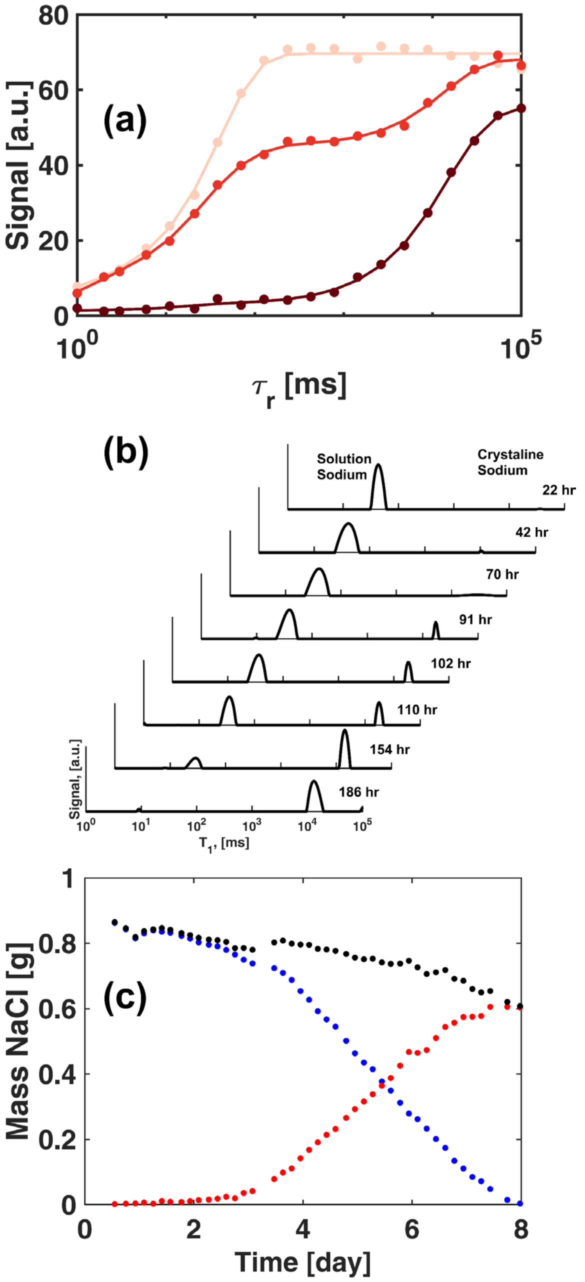

Fig. 4. (a) T_1 saturation recovery curves versus T_1 recovery delay, τ_r at three time points. Initially, (▬) the entire signal recovers over a short τ_r indicating that all sodium is in the solution. As deposition progresses, the recovery curves (▬) shows a signal component that recovers at a longer time. This component corresponds to the ^{23}Na crystals. After drying is complete, (▬) the entire signal recovers at the long recovery delay. (b) T_1 saturation recovery curves were processed using ILT to give T_1 relaxation time distributions. The short T_1 component, corresponding to solution ^{23}Na shows a reduction in signal intensity, while the long T_1 relaxation component shows increase. (c) The signal intensity resolved by T_1 as a function time during the process shows conversion of solution ^{23}Na to its crystalline form. Data points (●) correspond to solution NaCl, while data points (●) correspond to crystalline NaCl. Data points (●) represent the total NaCl within the sample.

These T_1 recovery curves were used in an inverse Laplace transform, as discussed in the Section 2.6 to give T_1 distributions shown in Figure 4(b). Sodium in salt crystals exhibits a much longer T_1 of ~13 seconds compared to solution sodium, which has a T_1 of 46 ms. The T_1 distributions show a decreasing contribution from the brine signal and an increasing contribution from the solid phase. Similar to the analysis of FID in Section 3.3, ^{23}Na MR signal resolved in T_1 were used to quantify sodium in both solution and crystalline forms, as presented in Figure 4(c). The trends observed from T_1 measurements are consistent with those obtained using FID analysis. This supports the reliability and quantitative validity of the results. However, due to fewer signal averages, T_1 measurements exhibit a higher noise level compared to FID data.

3.5 ^{1}H vs ^{23}Na imaging

Figure 5 shows the ^{23}Na and ^{1}H images at two time points during the evaporation/salt deposition process. At time 0.3 day, evaporation/salt deposition has not yet occurred yet. Therefore, both ^{23}Na and ^{1}H images in Figure 5(a) and (b) reflect brine content and show a capillary end effect. At $t = 3.3$ day, salt deposition has commenced. Sodium is transported toward the inlet of the sample where deposition occurs. The ^{23}Na image in Figure 5(c) shows a higher sodium content at the entrance of the sample. However, the ^{1}H image in Figure 5(d) shows a slightly higher ^{1}H content toward the outlet of the sample. This subtle gradient promotes capillary-driven flow to the inlet. This is a seemingly unexpected result, as the spatial distributions of ^{1}H and solution ^{23}Na show opposing trends across the sample. To meaningfully interpret these observations, a discussion on the profile of solution ^{23}Na concentration is required.

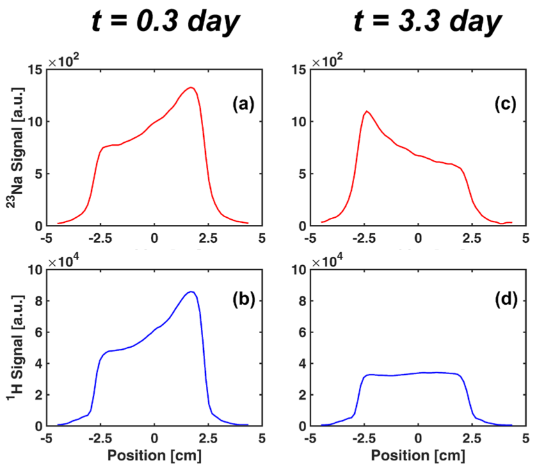

Fig. 5. (a) Solution ^{23}Na and (b) ^{1}H profiles at t = 0.3 day, immediately after the initial displacement. The capillary end effect is apparent. (c) Solution ^{23}Na and (d) ^{1}H profiles at t = 3.3 day when evaporation and deposition had stared. The solution ^{23}N profile shows a sodium concentration gradient toward the drying front at the core plug entrance. The ^{1}H profile shows a slightly reduced ^{1}H content at the drying front, causing transportation of water to the drying front. Day 3.3 is shortly after commencing of the salt deposition. Therefore, these profiles may still be evolving.

Using the variable field magnet, we can directly compare the signal intensities from the two nuclei without the complicated excitation/detection corrections that typically complicate such comparisons. However, to relate the signals to the molar quantities of each nucleus, corrections must still be applied for differences in gyromagnetic ratio and spin quantum number, as described by Eq. 4. After applying these corrections, the signal amplitudes, $|s|$ shown in Figure 5 yield the number of nuclei, N_H and N_{Na} for ^{1}H and ^{23}Na in arbitrary units, respectively. To convert the ratio of the number of nuclei to concentration, we first consider the number of ^{1}H spins per unit volume, given by:

$$\frac{n_H \cdot \rho_{brine}}{MW_{brine}}$$

where $n_H \cong 2$ for the number of hydrogen atoms per molecule of brine. ρ_{brine} is the density of the brine, MW_{brine} and is the molecular weight of the brine. Similarly, the number of sodium nuclei per unit volume is:

$$\frac{\rho_{brine} \cdot C_{Na}}{MW_{NaCl}}$$

where C_{Na} is the weight percent concentration of NaCl and MW_{NaCl} is the molecular weight of NaCl. C_{Na} is given by:

$$C_{Na} = \frac{N_H}{N_{Na}} \cdot \frac{n_H \cdot \rho_{brine}}{MW_{brine}} \cdot \frac{MW_{NaCl}}{\rho_{brine}} \qquad (5)$$

Figure 6 shows the sodium concentration at $t = 0.3$ and 3.3 day. Initially, the concentration is 8 wt%. This is the concentration used in preparing brine. Recovering the initial concentration of brine validates the quantification of sodium and hydrogen content from the MR measurements. At $t = 3.3$ days, the solution ^{23}Na shows a concentration gradient across the sample. The higher concentration at the inlet is consistent with the accumulation of salt crystals at this region.

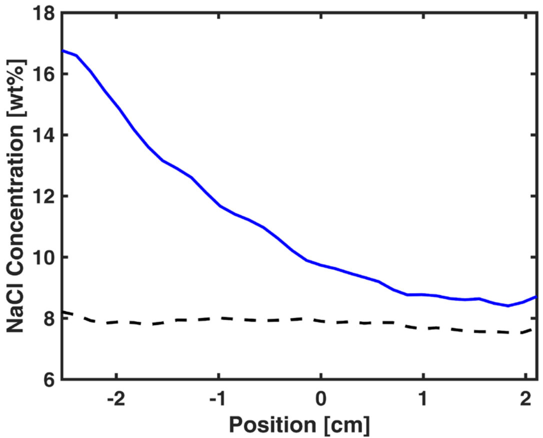

Fig. 6. (▪▪▪) ^{23}Na solution concentration at t = 0.3 day after initial brine displacement, before evaporation and salt deposition occur. The calculated concentration profile matches the prepared brine concentration used to saturate the core plug. (▬) ^{23}Na solution concentration at t = 3.3 day after evaporation has started. The higher concentration of NaCl at the drying front is a result of brine evaporation.

Returning to the opposing trends observed in the ^{1}H and ^{23}Na profiles in Figure 5, the slight decrease in ^{1}H signal indicates the brine saturation is slightly reduced at the inlet. This subtle gradient promotes capillary-driven flow of brine to the inlet, where it evaporates. Figure 6 shows that the sodium concentration is higher at the inlet. This condition promotes salt deposition. Continuous evaporation at the inlet establishes a saturation gradient, which drives capillary backflow. This backflow transports dissolved sodium toward the inlet, where salt precipitation occurs. This sequence represents the interplay between evaporation, capillary transport, and precipitation that governs salt deposition under the current experimental conditions. Currently, only two ^{1}H measurements were performed. To fully understand the phenomena, a series of interleaved ^{1}H and ^{23}Na measurements is recommended to monitor the brine as well as sodium dynamics.

3.6 Macroscopic Salt Deposition

Figure 7 shows 2D spatial distribution of salt deposition at the entrance face of the core plug after flow-through drying. The image reveals distinct spatial heterogeneity, with two prominent high intensity regions indicating localized accumulation of salt crystals. This non-uniform macroscopic distribution suggests that salt deposition is not solely governed by uniform evaporation or concentration gradients but is significantly influenced by the internal flow regime during drying.

The inlet face of the core plug, see the inset of Figure 2, shows the imprint of the inlet distributor after the experiment. This pattern does not correspond to the high-intensity regions in Figure 7. This discrepancy suggests that surface inspection alone does not reflect the salt deposition pattern. Figures 2 and 7 indicate that salt crystals accumulated slightly within the core, in regions close to the inlet.

The presence of salt rich zones raises important questions about the underlying pore scale heterogeneity of salt deposition. In addition to images showing macroscopic affects, at pore scale, MR relaxation lifetimes are sensitive to pore structure and fluid distribution. These relaxation lifetimes could be used to probe the relationship between salt crystallization and pore space geometry. Additional pore-scale information could be gained by incorporating spatially resolved ^{1}H T_2 relaxation measurements. This warrants further investigation.

These findings are highly relevant to understanding salt precipitation behavior in CO_2 storage operations, where salt accumulation can lead to significant permeability reduction and changes in rock porosity. CO_2 dissolution in the brine may impact the chemistry and physics of salt precipitation. Therefore, future research with CO_2, rather than inert N_2, is very advantageous. Furthermore, future direction for investigation of salt-out phenomenon may include controlled variation of key parameters such as thermodynamic conditions, salinity, flow rate, gas humidity, rock mineralogy, and pore structure, while measuring MR/MRI data, performing conventional effluent analysis, and evaluating permeability changes.

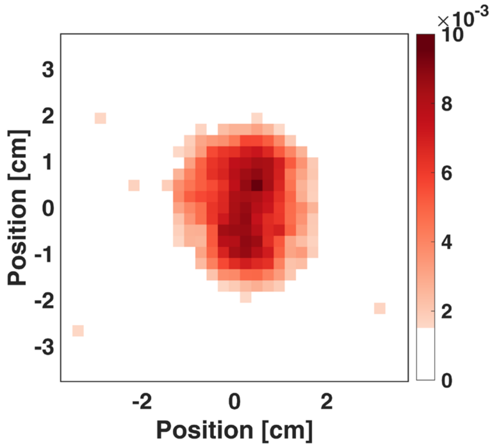

Fig. 7. 2D SPRITE image of crystalline ^{23}Na acquired after the drying process was complete. The image plane is transverse to the direction of gas flow. There is a spatial pattern showing two darker spots where salt deposition was more intense.

4 Conclusions

In this study, we demonstrate application of ^{23}Na MR/MRI to elucidate the water evaporation and salt precipitation phenomena during flow-through drying of porous media. Such studies are particularly relevant to CO_2 storage operations, where understanding the conditions in which salt precipitation impacts injectivity is critical for mitigation strategies and maintaining well injectivity.

Quantifying permeability changes during salt deposition is essential for evaluating the impact of salt precipitation on injectivity. Such analysis lies beyond the scope of this study. A comprehensive investigation would require systematic variation of parameters such as thermodynamic conditions, salinity, flow rate, and rock properties, with simultaneous permeability and MR/MRI measurements.

In this work, ^{23}Na and ^{1}H MR/MRI were employed to provide spatial and temporal data for drying and salt deposition in a Bentheimer sandstone. MR signal from sodium in solution and solid phase was resolved quantitatively using T_2* and T_1 relaxation time contrast. Consistent results from both methods and gravimetric measurement validated that the approach is quantitative throughout the drying process. We imaged solution ^{23}Na using Hybrid-SESPI and crystalline ^{23}Na using DHK SPRITE method.

A clear sequence of processes was observed. Initial displacement of brine by gas flow, followed by evaporation and capillary-driven backflow, and ultimately salt precipitation localized at the core entrance. The solution sodium profile evolved from a capillary end-effect pattern to a reversed concentration gradient toward the drying front at the inlet of the core plug. Notably, the salt deposition rate remained approximately constant during most of the experiment, indicating a quasi-steady evaporation regime confined to a localized drying front near the sample inlet.

The spatial mismatch between ^{1}H and solution ^{23}Na profiles was attributed to capillary backflow, which transported sodium toward the inlet, leading to the observed accumulation of sodium crystals in that region. This highlights the complex interplay of fluid transport and phase change in porous media under drying conditions.

The methods presented in this work offer new insights into salt precipitation dynamics relevant to CO_2 storage in saline aquifers. Unlike most studies that primarily rely on X-ray CT, the ^{23}Na MR/MRI approach enables the use of natural brines and salts while providing spatially resolved information on solute concentration. These capabilities that are not readily accessible with X-ray CT.

Authors acknowledge TotalEnergies and Green Imaging Technologies for financial support. We thank NSERC for an Alliance award grant [ALLRP 571885-21] and a Discovery grant [2022-04003].

References

1. E. Terrenoire, D.A. Hauglustaine, T. Gasser, O. Penanhoat, Environ. Res. Lett. **14**(8) (2019)
2. A. Bashir, M. Ali, S. Patil, M. Aljawad, M. Mahmoud, D. Al-Shehri, H. Hoteit, M. Kamal, Earth Sci. Rev. **249**, 104672 (2024)
3. X. Sun, K. Liu, S. An, H. Hellevang, Y. Cao, J. Alcalde, A. Travé, G. Yuan, C. Deng, E. Gomez-Rivas, Geoenergy. Sci. Eng. **244**, 213451 (2025)
4. R. Jasinski, W. Sablerolle, M. Amory, SPE Annual Technical Conference and Exhibition, SPE-38767-MS (1997)
5. W. Kleinitz, M. Koehler, G. Dietzsch, SPE European Formation Damage Conference, SPE-68953-MS (2001)
6. P. Tawiah, J. Duer, S.L. Bryant, S. Larter, S. O'Brien, M. Dong, Int. J. Greenh. Gas Con. **92**, 102843 (2020)
7. K. Pruess, J. García, Environ. Geol. **42**, 282-295 (2002)
8. H. Ott, J. Snippe, K. de Kloe, Int. J. Greenh. Gas Con. **105**, 103233 (2021)
9. H. Ott, S.M. Roels, K. de Kloe, Int. J. Greenh. Gas Con. **43**, 247-255 (2015)
10. N. Muller, R. Qi, E. Mackie, K. Pruess, M.J. Blunt, Energy Procedia **1**, 3507-3514 (2009)
11. H. Ott, K. de Kloe, F. Marcelis, A. Makurat, Energy Procedia **4**, 4425-4432 (2011)
12. K. Pruess, N. Müller, Water Resour. Res. **45**(3) (2009)
13. Y. Wang, T. Luce, C. Ishizawa, M. Shuck, K. Smith, H. Ott, M. Appel, International Symposium of the Society of Core Analysts, SCA2010-18 (2010)
14. M. Zeidouni, M. Pooladi-Darvish, D. Keith, Int. J. Greenh. Gas Con. **3**, 600-611 (2009)
15. G. Bacci, A. Korre, S. Durucan, Energy Procedia **4**, 4450-4456 (2011)
16. I.H. Falcon-Suarez, K. Livo, B. Callow, H. Marin-Moreno, M. Prasad, A.I. Best, Sci. Rep. **10**, 16472 (2020)
17. R. Miri, H. Hellevang, Int. J. Greenh. Gas Con. **51**, 136-147 (2016)
18. M. Kim, A. Sell, D. Sinton, Lab Chip **13**, 2508-2518 (2013)
19. R. Miri, R. van Noort, P. Aagaard, H. Hellevang, Int. J. Greenh. Gas Con. **43**, 10-21 (2015)
20. M.N. Rad, N. Shokri, Water Resour. Res. **50**, 9020-9030 (2014)
21. D. Akindipe, S. Saraji, M. Piri, Adv. Water Resour. **155**, 104011 (2021)
22. D. Akindipe, S. Saraji, M. Piri, Int. J. Greenh. Gas Con. **121**, 103790 (2022)
23. Y. Wang, E. Mackie, J. Rohan, T. Luce, R. Knabe, and M. Appel, International Symposium of the Society of Core Analysts, SCA2009-25 (2009)
24. J. Mitchell, E.J. Fordham, Rev. Sci. Instrum. **85**(11), 111502 (2014)
25. M.S. Zamiri, N. Ansaribaranghar, F. Marica, A.R. Aguilera, D. Green, C. Caubit, B. Nicot, B.J. Balcom, International Symposium of the Society of Core Analysts, SCA2024-1032 (2024),
26. R. Rajeev, N. Ansaribaranghar, A.R. Aguilera, F. Marica, L. Romero-Zerón, B.J. Balcom, J. Magn. Reson. **369**, 107811 (2024)
27. K. Deka, B. MacMillan, G.R. Ziegler, A.G. Marangoni, B. Newling, B.J. Balcom, Food Res. Int. **39**(3) 365-371 (2006)

28. M.S. Zamiri, F. Marica, L. Romero-Zerón, B.J. Balcom, Chem. Eng. J. **428**, 131042 (2022)
29. C.E. Muir, B.J. Balcom, Ann. R. NMR S. **77** 81-113 (2012)
30. N. Ansaribaranghar, M.S. Zamiri, F. Pairoys, V. Fernandes, L. Romero-Zerón, F. Marica, A.R Aguilera, D. Green, B. Nicot, B.J. Balcom, International Symposium of the Society of Core Analysts, SCA2024-1064 (2024)
31. N. Ansaribaranghar, M.S. Zamiri, L. Romero-Zerón, F. Marica, A.R. Aguilera, D. Green, B. Nicot, B.J. Balcom, Petrophysics **66**(1), 169-182 (2025)
32. N. Ansaribaranghar, M.S. Zamiri, L. Romero-Zerón, F. Marica, A.R. Aguilera, D. Green, B. Nicot, B.J. Balcom, Petrophysics **66**(1), 155-168 (2025)
33. M. Li, P. Kortunov, A. Lee, F. Marica, B.J. Balcom, Chem. Eng. J. 500, 157100 (2024)
34. E. Mark Haacke, Robert W. Brown, Michael R. Thompson, Ramesh Venkatesan, *Magnetic Resonance Imaging: Physical Principles and Sequence Design* (Wiley-Liss, 1999)
35. B.J. Balcom, R.P. Macgregor, S.D. Beyea, D.P. Green, R.L. Armstrong, T.W. Bremner, J. Magn. Reson. Ser. A. **123**(1) 131-134 (1996)
36. B. MacMillan, P. Szomolanyi, D. Matheson, B.J. Balcom, J. Magn. Reson. **165**(2) 219-229 (2003)
37. J. Guo, B. MacMillan, M.S. Zamiri, B.J. Balcom, J. Magn. Reson. **328**, 107005 (2021)

38. Y.-Q. Song, L. Venkataramanan, M.D. Hürlimann, M. Flaum, P. Frulla, C. Straley, J. Magn. Reson. **154**, 261-268 (2002).
39. Y. Peysson, L. Andŕe, M. Azaroual, Int. J. Greenh. Gas Con. **22**, 291-300 (2014)
40. L. Andŕe, Y. Peysson, M. Azaroual, Int. J. Greenh. Gas Con. **22**, 301-312 (2014)